Ultrasonics 95 (2019) 52–62

Contents lists available at ScienceDirect

Ultrasonics

journal homepage: www.elsevier.com/locate/ultras

Guided acoustic waves at the intersection of interfaces and surfaces

P.D. Pupyrev[a,b], I.A. Nedospasov[c], A.P. Mayer[b,*]

[a] Prokhorov General Physics Institute of the Russian Academy of Sciences, Vavilova Str. 38, 119991 Moscow, Russia
[b] HS Offenburg – University of Applied Sciences, Klosterstr. 14, 77723 Gengenbach, Germany
[c] Kotelnikov Institute of Radio Engineering and Electronics of the Russian Academy of Sciences, Mokhovaya Str. 11-7, 125009 Moscow, Russia

ARTICLE INFO

Keywords:
Guided waves
Surface acoustic waves
Wedge waves
Finite element method

ABSTRACT

In numerical calculations, guided acoustic waves, localized in two spatial dimensions, have been shown to exist and their properties have been investigated in three different geometries, (i) a half-space consisting of two elastic media with a planar interface inclined to the common surface, (ii) a wedge made of two elastic media with a planar interface, and (iii) the free edge of an elastic layer between two quarter-spaces or two wedge-shaped pieces of a material with elastic properties and density differing from those of the intermediate layer.

For the special case of Poisson media forming systems (i) and (ii), the existence ranges of these 1D guided waves in parameter space have been determined and found to strongly depend on the inclination angle between surface and interface in case (i) and the wedge angle in case (ii). In a system of type (ii) made of two materials with strong acoustic mismatch and in systems of type (iii), leaky waves have been found with a high degree of spatial localization of the associated displacements, although the two materials constituting these structures are isotropic.

Both the fully guided and the leaky waves analyzed in this work could find applications in non-destructive evaluation of composite structures and should be accounted for in geophysical prospecting, for example.

A critical comparison is presented of the two computational approaches employed, namely a semi-analytical finite element scheme and a method based on an expansion of the displacement field in a double series of special functions.

1. Introduction

Guided acoustic waves have found applications in various fields of science and technology [1]. Since their discovery, surface acoustic waves (SAWs) in homogeneous media and in layered structures, and interface waves between two solid media or between a solid and a liquid have been investigated and applied in geophysical contexts. They find increasing attention in seismics and geophysical prospecting [2,3]. Their presence influences scattering of bulk waves and therefore, knowledge about them is required even if they are not directly employed in seismic exploration. Since the nineteen sixties, SAWs are used in signal processing devices and various types of sensors [4], and they play an increasingly important role in non-destructive evaluation [5], also in connection with nonlinearity [6]. More recently, other types of guided acoustic waves have moved into the focus, too, like plate modes and acoustic modes of pipes, for example, which have found applications in nondestructive testing and structural health monitoring [7]. In a medical application, guided acoustic waves were even excited in cortical bone ([8] and references therein to earlier work). Obvious advantages of using guided waves instead of bulk acoustic waves in these applications is the absence (or at least a strong reduction) of diffraction losses and an enhanced sensitivity to geometric features and specific kinds of defects, depending on the displacement patterns of the guided waves, which are normally much more complex than those of bulk waves. An effective use of guided acoustic waves in technical applications requires knowledge about their properties, which this work is intended to make a contribution to.

Acoustic guided waves in solids and liquids may be categorized in various ways, for example with respect to their dimensionality. The strain field associated with a guided wave may be confined along one spatial direction, but in the remaining two directions, the waveguide exhibits translational invariance (apart from gradual changes that the term “wave guiding” normally refers to). Therefore, the acoustic waves propagating in such a waveguide appear as superpositions of “elementary waves,” which have the character of plane waves with two-component wave-vectors concerning their dependence on the coordinates in the plane of translational invariance. Such guided waves we shall call 2D. In contradistinction to this case, we shall use the term

---

[*] Corresponding author.
E-mail address: andreas.mayer@hs-offenburg.de (A.P. Mayer).

https://doi.org/10.1016/j.ultras.2019.03.002
Received 6 November 2018; Received in revised form 28 February 2019; Accepted 1 March 2019

1D for guided waves that have a strain field confined in two spatial dimensions in a waveguide with translational invariance along the third direction. Such 1D guided waves may be decomposed in “elementary waves” characterized by a 1D wave-vector.

A second way of categorizing guided acoustic waves leads to the following two groups. The first group consists of waves with associated strain fields that fill the whole solid/liquid structure which itself is spatially confined. It encompasses most of the acoustic waves in rods, pipes and plates. In the second group, the structure the waves are propagating in is infinitely extended in one or both spatial directions vertical to the propagation direction of the guided waves, and the displacement field associated with these waves decays to zero exponentially along this (these) direction(s). The simplest 2D examples for this kind of guided acoustic waves are Rayleigh waves propagating at the surface of a homogeneous half-space, or Stoneley waves localized at the interface between two solid elastic media. Wedge acoustic waves that are localized at the tip of an infinite elastic wedge are 1D examples of this kind. Such systems also allow for the occurrence of leaky waves which radiate energy into the elastic medium away from the waveguide and their amplitude decreases along the propagation direction as a result of this energy loss. (For a recent review see [9] and references therein.) The work reported here pertains to 1D guided waves of the latter type. Of the categories presented by Oliner in Fig. 5.1 of [10], the waveguide structures (a–e) are of this second kind. However, there is an important difference between these examples, considered in [10], and the waveguide structures we are concerned with here. In these geometries, 1D acoustic wave-guiding at the surface of an elastic medium is realized by modifying a finite region of the cross section of the half space (a plane normal to the surface of the half-space) to localize a surface wave in the lateral direction. This is not the case in the structures we are concerned with (Fig. 1). The systems of Fig. 1(a–d) involve two elastic media and lead to 1D guided acoustic waves at the intersection line between the surface(s) of and the interface between these two media. Since the geometry of these systems does not define any length scale, these guided waves are non-dispersive in the case of a perfect (“welded”) contact between the media.

It was recently shown that 1D guided acoustic waves exist at the intersection line between the interface and the common surface of two quarter-spaces (Fig. 1a). They have been termed Rayleigh-Stoneley waves [11]. While in isotropic media, Rayleigh waves exist for all physical values of the Poisson ratio, Stoneley waves do not exist for all combinations of Lamé constants and densities of two adjacent media. For two Poisson media (i.e. isotropic elastic media with their two Lamé constants being equal), Scholte [12] determined their existence area in the two-dimensional parameter space. In [11] it was found that the existence area of the 1D Rayleigh-Stoneley waves, propagating in the geometry of Fig. 1a, is a small sub-set of the existence area for Stoneley waves. In the following, we shall investigate the existence and properties of 1D guided acoustic waves in the geometry of Fig. 1b, where the interface between the two coupled elastic media is no longer vertical to the surface. A second generalization of the system of Fig. 1a is shown in Fig. 1c.

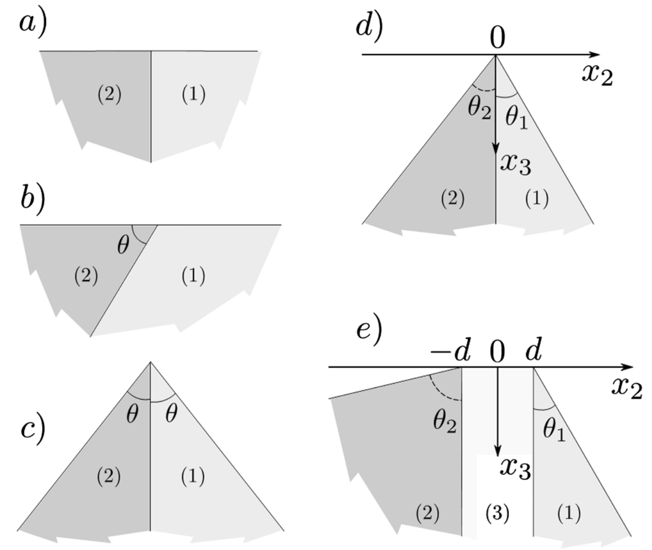

Fig. 1. Geometries for guided waves considered in this work. Propagation along x_1-direction.

Our main goal for the two geometries Fig. 1b and c is to investigate the dependence of the domain of existence of 1D guided waves in parameter space on the inclination angle θ. For certain combinations of isotropic materials and angles θ_1, θ_2, acoustic waves propagating in the system Fig. 1d are studied in view of the existence and properties of leaky wedge waves. Leaky wedge acoustic waves were first discovered in homogeneous anisotropic wedges in laser-ultrasound experiments [13] and have recently been found in numerical simulations to also exist in wedges made of two isotropic materials [14].

In their study of acoustic waves at a planar fracture [15], Abell and Pyrak-Nolte have relaxed the “welded contact” boundary conditions at the interface between the two quarter-spaces in Fig. 1a and introduced interface stiffnesses. This widens the existence domain of 1D guided acoustic waves – they were found to exist even for quarter-spaces of equal materials – and also renders them dispersive.

The coupling between the two quarter-spaces in Fig. 1a via interface stiffnesses or other effects, may be regarded as being mediated by an interface layer having its own mechanical properties. We have therefore considered the system shown in Fig. 1e, where the angles θ_1, θ_2 may, but need not take the value 90°. This layer may represent a transition zone in a fracture, that may be filled with a softer material, a glue, or the system in Fig. 1e may represent part of the edge of a composite material. The thickness $2d$ of this interface layer introduces dispersion to guided waves propagating in this system.

For the systems in Fig. 1, numerical searches have been carried out of 1D guided acoustic waves that propagate along the x_1-direction. The aim of this search is to find such waves and to investigate their properties with regard to applications in non-destructive evaluation and geophysics, for example. The guided modes of the systems in Fig. 1 may at least partly be regarded as generalizations of wedge acoustic waves, i.e. acoustic waves guided by the apex line of a homogeneous elastic wedge. The theoretical methods we use for our purpose are essentially those applied already in the discovery and earliest studies of wedge waves, namely a semi-analytical finite element method (FEM) [16,17] and an approach based on an expansion of the displacement field in a double series of special functions particularly suitable for the geometries considered [18–20]. They have been further developed and adapted to the systems considered here. Especially, they have been extended to include a source that simplifies the search for leaky waves. Both theoretical methods have been used in this study and their results have been compared to each other in order to avoid convergence and accuracy problems.

In Section 2, the two numerical approaches are briefly described and their convergence demonstrated for an example. Subsequently, the systems in Fig. 1b and 1c are considered for the case of two Poisson media. It is shown how the range of existence of 1D guided waves changes with varying angle θ. In the following section, acoustic wave propagation in a wedge consisting of two isotopic elastic media of the form Fig. 1d is studied, and it is shown that leaky wedge waves exist in this system. The dependence of their speed and tip localization on angles θ_1, θ_2 is presented for a specific combination of materials. Finally, a new type of acoustic 1D guided waves is presented in the system of Fig. 1e which may be regarded as a generalization of the elastic modes localized at the edge of an elastic plate.

2. Numerical methods

In each elastic medium of those occurring in the systems of Fig. 1, the displacement field $u_\alpha(x_1, x_2, x_3, t)$ has to satisfy the equation of motion

$$\rho\frac{\partial^2}{\partial t^2}u_\alpha = \frac{\partial}{\partial x_\beta}\sigma_{\alpha\beta}, \tag{2.1}$$

where ρ is the mass density of and $\sigma_{\alpha\beta}$ are the components of the stress tensor in the corresponding medium with the constitutive equation

$$\sigma_{\alpha\beta} = C_{\alpha\beta\,\mu\nu}\frac{1}{2}\left(\frac{\partial}{\partial x_\nu}u_\mu + \frac{\partial}{\partial x_\mu}u_\nu\right), \tag{2.2}$$

where $C_{\alpha\beta\,\mu\nu}$ are elastic constants. Cartesian indices are denoted by Greek letters. In (2.1) and (2.2) and the following equations, summation over repeated Cartesian indices is implied. (2.1) is supplemented by boundary conditions at surfaces, interfaces and at infinity. At interfaces, we require continuity of the displacement field and of the quantities $N_\beta(x_2, x_3)\,\sigma_{\alpha\beta}(x_1, x_2, x_3, t)$, where $\mathbf{N}(x_2, x_3)$ is a vector normal to the interface at position (x_1, x_2, x_3). At a free surface, $N_\beta(x_2, x_3)\,\sigma_{\alpha\beta}(x_1, x_2, x_3, t)$ has to vanish, where $\mathbf{N}(x_2, x_3)$ is now a vector normal to the surface at position (x_1, x_2, x_3). Alternatively, we set

$$N_\beta(x_2, x_3)\,[\sigma_{\alpha\beta}(x_1, x_2, x_3, t) - \sigma^{(\text{ext})}_{\alpha\beta}(x_1, x_2, x_3, t)] = 0, \tag{2.3}$$

where $\sigma^{(\text{ext})}_{\alpha\beta}$ is an external time-dependent stress (source) applied to a certain area of the surface. At infinity, the displacement field has to vanish or Sommerfeld radiation conditions are imposed.

Because of translational invariance of our systems along the x_1-direction, we may seek solutions of the above-defined boundary value problem of the form

$$u_\alpha(x_1, x_2, x_3, t) = e^{i(kx_1-\omega t)}U_\alpha(x_2, x_3|k) \tag{2.4}$$

in the absence of a time-dependent external source. The stress tensor may likewise be written as

$$\sigma_{\alpha\beta}(x_1, x_2, x_3, t) = e^{i(kx_1-\omega t)}T_{\alpha\beta}(x_2, x_3|k). \tag{2.5}$$

The Eqs. (2.1) and (2.2) then take the forms

$$\rho\omega^2U_\alpha(x_2, x_3|k) = -D_\beta(k)T_{\alpha\beta}(x_2, x_3|k), \tag{2.6}$$

$$T_{\alpha\beta}(x_2, x_3|k) = C_{\alpha\beta\,\mu\nu}D_\nu(k)U_\mu(x_2, x_3|k), \tag{2.7}$$

with the operator $D_\alpha(k) = \delta_{\alpha1}ik + (1-\delta_{\alpha1})\partial/\partial x_\alpha$ and $\delta_{\alpha\beta}$ is the Kronecker symbol. The Ansatz (2.4) remains valid in the presence of an external stress of the form

$$\sigma^{(\text{ext})}_{\alpha\beta}(x_1, x_2, x_3, t) = e^{i(kx_1-\omega t)}T^{(\text{ext})}_{\alpha\beta}(x_2, x_3|k, \omega). \tag{2.8}$$

2.1. Semi-analytical finite element approach

The linear boundary value problem specified above has been solved approximately with a two-dimensional iso-parametric finite element scheme employing eight-node elements. In the absence of an external source, the frequencies and displacement patterns of 1D guided modes were identified by solving a generalized eigenvalue problem of the form

$$\sum_{\ell'=1}^{N}\,[\omega^2M^{(\text{mass})}_{\alpha\ell\,\beta\ell'} - M^{(\text{stiff})}_{\alpha\ell\,\beta\ell'}(k)]\,\hat{U}_{\beta\ell'} = 0 \tag{2.9}$$

with elements $M^{(\text{mass})}_{\alpha\ell\,\beta\ell'}$ of the global mass matrix and $M^{(\text{stiff})}_{\alpha\ell\,\beta\ell'}(k)$ of the global wave-vector-dependent stiffness matrix. $\hat{U}_{\beta\,\ell}$ is the displacement of node ℓ in the x_β direction and the sum in (2.9) runs over the N nodes of the total mesh.

In case of an external source of the form (2.8), a non-zero right-hand side in (2.9) occurs, and the resulting inhomogeneous linear system of equations is solved for given frequency ω and wave-vector k. In the presence of a source, perfectly matched layers (PML) have been introduced at large distances from the 1D waveguide in order to avoid reflections of bulk, surface or interface waves from surfaces appearing due to truncation of an infinite system. These surfaces become interfaces with the PML regions and are always parallel to coordinate planes in our systems (Fig. 2) apart from sharp-angle wedges (see below). The PML is implemented following [21]. In the PML regions, the elastic moduli $C_{\alpha\beta\,\mu\nu}$ of the material in contact with the PML are replaced by $C_{\alpha\beta\,\mu\nu}\tilde{z}z_\beta^{-1}z_\nu^{-1}$ and its density ρ by $\rho\,\tilde{z}$ where $z_\alpha(x_\alpha) = 1 - i\sigma_\alpha(x_\alpha - x_\alpha^{(\text{interface})})^2$ and $x_\alpha^{(\text{interface})}$ defines the position of the interface. Fig. 2a shows an example system consisting of two elastic media. The regions 1,…,6 are PMLs. In regions 1 and 6, only σ_2 is non-zero, in regions 3 and 4, only σ_3 is non-zero, and in regions 2 and 5, both σ_2 and σ_3 are non-zero. The parameters σ_α are optimized to suppress reflections. Furthermore, $\tilde{z} = z_1 z_2 z_3$. In connection with leaky waves in systems of the type of Fig. 1d with small angles θ_1, θ_2, meshes were used with elements arranged in a circular order and the PMLs were adapted to this geometry in order to achieve better performance. For a test case, the same velocity of the leaky wave was obtained for the circular mesh and for a mesh with PMLs arranged as in Fig. 2a.

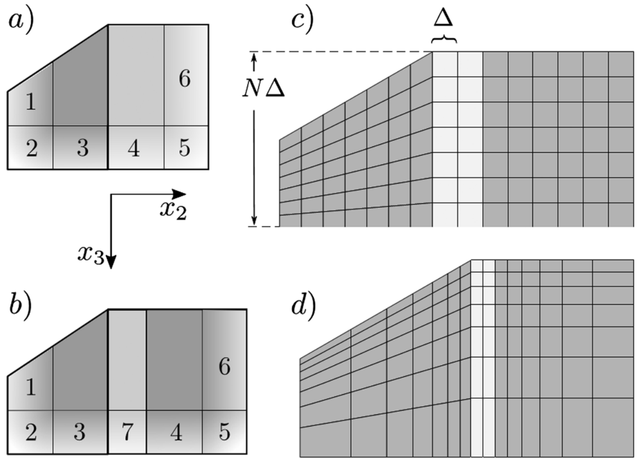

Fig. 2. Example systems, consisting of two elastic media and PMLs 1,…,6 (a), and consisting of three elastic media and PML regions 1,…,7 (b). Three elastic media with linear mesh (c) and logarithmic mesh (d).

In systems consisting of three elastic media, only those cases were considered, where the medium in the center has bulk wave velocities smaller than those of the other media (on the right and left of the center medium). These cases allowed for a simplification if only such solutions were investigated that are subsonic with respect to media (1) and (2). Here it was sufficient to place a PML underneath the center region only (area 7 in Fig. 2b).

2.2. Laguerre-Legendre function method

An alternative method for the determination of the frequencies and displacement patterns of 1D guided acoustic modes in the systems shown in Fig. 1 is based on an expansion of the quantities U_α in a double series of special functions that are appropriate for the geometry considered. This method was applied to homogeneous elastic wedges [18,19,22], including anisotropy [23–25], piezo-electricity [23,24] and nonlinear effects [26], and to edges of elastic plates [20]. Recently, it was extended to two elastic quarter-spaces in "welded" contact [11] and a weak contact involving interface stiffnesses [15] (Fig. 1a). It was also applied to 1D guided modes propagating along the intersection line between to fracture planes [27].

In this work, it is further developed to account for external stress and applied to systems of the types Figs. 1d and e. The latter may be regarded as a combination of two wedges and a plate. We demonstrate this approach first at the system Fig. 1d, i.e. two wedges made of different materials in "welded" contact. The presentation of the derivations largely follows that given in [11] with new extensions being inserted. In order to simplify notation, we denote in the following the Cartesian spatial coordinates by x, y, z instead of x_1, x_2, x_3.

2.2.1. Determination of localized modes for two media in contact

In both media, the functions U_α are represented as linear combinations of products of Laguerre functions in the following way [19]:

$$U_\alpha^{(1/2)}(y, z|k) = \sum_{m,n=0}^{\infty} a_{mn}^{(\alpha,1/2)}\, \phi_m(k\eta_{1/2}(y, z))\, \phi_n(k\zeta_{1/2}(y, z)), \tag{2.10}$$

where

$$\begin{pmatrix} x \\ \eta_{1/2}(y, z) \\ \zeta_{1/2}(y, z) \end{pmatrix} = \mathbf{B}_{1/2} \begin{pmatrix} x \\ y \\ z \end{pmatrix}. \tag{2.11}$$

In (2.11) and further equations, the notation (1/2) refers the two wedges 1 and 2 with wedge angles θ_1, θ_2. The matrices $\mathbf{B}_{1/2}$ represent linear transformations mapping the cross sections of the two wedges in the y-z plane into the same rectangular area $[0, \infty) \times [0, \infty)$ in the η-ζ plane. This mapping can be decomposed into a sequence of three simple transformations, schematically shown in Fig. 3:

$$\mathbf{B}_{1/2} = \mathbf{S}_{1/2}\, \mathbf{R}(\gamma_{1/2})\, \mathbf{\Gamma}_{1/2}. \tag{2.12}$$

Here $\mathbf{\Gamma}_2$ stands for the reflection at the x-z plane and $\mathbf{\Gamma}_1$ is the identity operation. Subsequently, $\mathbf{R}(\gamma_{1/2})$ rotates the two wedges around the x-axis into the symmetric orientations as shown in Fig. 3. The rotation angles are $\gamma_{1/2} = \pi/4 - \theta_{1/2}/2$. Explicitly:

$$\mathbf{\Gamma}_{1/2} \begin{pmatrix} 1 & 0 & 0 \\ 0 & \pm 1 & 0 \\ 0 & 0 & 1 \end{pmatrix}, \ \mathbf{R} = \begin{pmatrix} 1 & 0 & 0 \\ 0 & \cos(\gamma) & \sin(\gamma) \\ 0 & -\sin(\gamma) & \cos(\gamma) \end{pmatrix}. \tag{2.13}$$

Finally, $\mathbf{S}$ is a combination of a deformation of the symmetrically oriented wedge into a rectangular wedge and a coordinate stretching, governed by the factors a_c, b_c:

$$\mathbf{S}_{1/2} = \begin{pmatrix} 1 & 0 & 0 \\ 0 & a_c^{(1/2)} & -a_c^{(1/2)}\tan(\gamma_{1/2}) \\ 0 & -b_c^{(1/2)}\tan(\gamma_{1/2}) & b_c^{(1/2)} \end{pmatrix}. \tag{2.14}$$

Such factors had been introduced earlier by Sharon et al. [22] to enhance convergence of wedge wave speeds with increasing number of Laguerre functions for sharp-angle wedges. Here, they are needed to ensure that points on the x_3-axis, i.e. at the interface between the two wedges, are mapped to the same point on the ζ-axis by the two linear transformations $\mathbf{B}_{1/2}$.

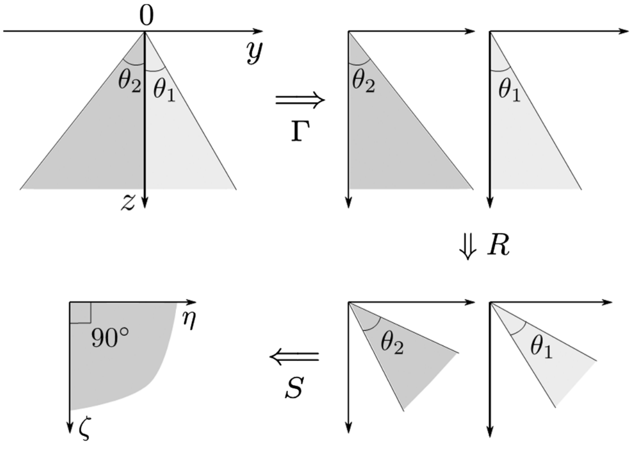

Fig. 3. Decomposition of linear mapping **B**.

The normalized Laguerre functions $\phi_n(\xi)$ are defined in the same way as in [18]. $a_{mn}^{(\alpha,1/2)}$ are expansion coefficients in the corresponding areas of the composite wedge's cross sections. Their values depend on the material constants of the two media in contact. These representations are now inserted into the equations of motion in the two media, which are then multiplied by $\phi_p(k\eta_{1/2}(y, z))\, \phi_q(k\varsigma_{1/2}(y, z))$ in the corresponding media. Integration over the corresponding cross-sectional areas and subsequently an integration by parts yields the equations

$$\sum_{m,n=0}^{\infty} \frac{1}{\det(\mathbf{S}_{1/2})} (M_{pq,mn}^{(\alpha\mu,1/2)} - \rho_{1/2}\, v^2\, \delta_{\alpha\mu}\, \delta_{pm}\, \delta_{qn})\, a_{mn}^{(\mu,1/2)} = \tau_q^{(\alpha,1/2)}, \tag{2.15}$$

where $v = \omega/k$ and we have introduced the matrices

$$M_{pq,mn}^{(\alpha\mu,1/2)} = \int_0^\infty \int_0^\infty [\tilde{D}_{\beta'}(k)\phi_p(k\eta)\phi_q(k\zeta)]^*\, \tilde{C}_{\alpha\beta'\,\mu\nu'}^{(1/2)} [\tilde{D}_{\nu'}(k)\phi_m(k\eta)\phi_n(k\zeta)]\, d\eta\, d\zeta, \tag{2.16}$$

which are independent of k. In (2.16) we have defined the operator $\tilde{D}_\beta = (ik, \partial/\partial\eta, \partial/\partial\zeta)_\beta$ and the transformed elastic constants $\tilde{C}_{\alpha\beta'\mu\nu'}^{(1/2)} = B_{\beta'\beta}^{(1/2)} B_{\nu'\nu}^{(1/2)} C_{\alpha\beta\,\mu\nu}^{(1/2)}$. In addition, we have made use of the fact that with the definition of the Laguerre functions used here, $\phi_n(0) = 1,\ \ n = 0, 1, 2, \ldots$ The quantities

$$\tau_n^{(\alpha,1/2)} = \int_0^\infty \phi_n(kb_c^{(1/2)}\chi(\gamma_{1/2})z)\, N_\beta^{(1/2)}\ T_{\alpha\beta}^{(1/2)}(0, z|k)\, dz, \tag{2.17}$$

occurring in (2.15), will be called "stress amplitudes at the interface." They are independent of k, too. In (2.17), $\chi(\gamma) = \cos(2\gamma)/\cos(\gamma)$. $N_\beta^{(1/2)} = \mp\delta_{\beta 2}$ are the out-of-plane normals of the interface and $\exp(ikx - \omega t)\, T_{\alpha\beta}^{(1/2)}(y, z|k)$ are the stress tensor components in medium 1/2. Choosing the factors $b_c^{(1/2)}$ such that

$$b_c^{(1)}\chi(\gamma_1) = b_c^{(2)}\chi(\gamma_2), \tag{2.18}$$

inserting $N_\beta^{(1/2)}$ and using the boundary condition $T_{\alpha\beta}^{(1)}(0, z|k) = T_{\alpha\beta}^{(2)}(0, z|k)$, we obtain:

$$\tau_n^{(\alpha,1)} = -\tau_n^{(\alpha,2)}. \tag{2.19}$$

Similarly, "displacement amplitudes at the interface,"

$$U_n^{(\alpha,1/2)} = k\int_0^\infty \phi_n(kb_c^{(1/2)}\chi(\gamma_{1/2})z)\, U_\alpha^{(1/2)}(0, z|k)\, dz, \tag{2.20}$$

are defined, which are related to the expansion coefficients $a_{mn}^{(\alpha,1/2)}$ in media 1 and 2 via

$$U_n^{(\alpha,1/2)} = \frac{1}{b_c^{(1/2)}\,\chi(\gamma_{1/2})} \sum_{m=0}^{\infty} a_{mn}^{(\alpha,1/2)}. \tag{2.21}$$

Here, the normalization of the Laguerre functions has been made use of. The boundary conditions at the interface and (2.18) imply

$$U_n^{(\alpha,1)} = U_n^{(\alpha,2)}. \tag{2.22}$$

We now proceed as in [11]. The stress and strain amplitudes at the interface are related to each other by eliminating the expansion coefficients $a_{mn}^{(\alpha,1/2)}$ from the above system of equations to yield:

$$U_n^{(\alpha,2)} = -\frac{\det(\mathbf{S}_1)}{b_c^{(1)}\,\chi(\gamma_1)} \sum_{q=0}^{\infty} G_{nq}^{(\alpha\beta,1)}(v^2)\, \tau_q^{(\beta,2)}, \tag{2.23}$$

$$U_n^{(\alpha,2)} = \frac{\det(\mathbf{S}_2)}{b_c^{(2)}\,\chi(\gamma_2)} \sum_{q=0}^{\infty} G_{nq}^{(\alpha\beta,2)}(v^2)\, \tau_q^{(\beta,2)}. \tag{2.24}$$

From the secular equation

$$\det[\mathbf{G}^{(1)-1}(v^2)/\det(\mathbf{S}_1) + \mathbf{G}^{(2)-1}(v^2)/\det(\mathbf{S}_2)] = 0, \tag{2.25}$$

resulting from the homogeneous linear system of equations (2.23) and (2.24), the phase velocities of the guided modes are determined. Here, $\mathbf{G}^{(1/2)-1}$ denotes the inverse of the matrix $\mathbf{G}^{(1/2)}$ with matrix elements $G_{nq}^{(\alpha\beta,1/2)}$. These matrices are determined approximately via the spectral representation of the matrices $\mathbf{M}^{(1/2)}$ defined in (2.16) after truncation of the series (2.10),

$$G_{nq}^{(\alpha\beta)}(v^2) = \sum_{j=1}^{j_{\max}} \frac{Q_n^{(\alpha)}(j)\, Q_q^{(\beta)*}(j)}{\lambda(j) - \rho v^2}, \tag{2.26}$$

where

$$Q_n^{(\alpha)}(j) = \sum_{m=0}^{m_{\max}} V_{mn}^{(\alpha)}(j) \tag{2.27}$$

and $V_{mn}^{(\alpha)}(j)$ are the components of the j-th eigenvector with corresponding eigenvalue $\lambda(j)$ of the matrix $\mathbf{M}$ with components $M_{pq,mn}^{(\alpha\beta)}$. The upper bound $j_{\max}$ of the summation index on the right-hand side of (2.26), i.e. the number of eigenvalues of $\mathbf{M}$, is equal to $3\,(m_{\max}+1)(n_{\max}+1)$, and $m_{\max}$, $n_{\max}$ are the upper bounds of the indices m, n in the double series (2.10).

2.2.2. External source

We now introduce an external time-dependent stress of the form (2.8) on the surface of wedge 1. As a consequence, not all components $T_{\alpha\beta}\tilde{N}_\beta$, $\alpha = 1, 2, 3$, of the traction vector vanish simultaneously at the half plane $y = z\tan(\theta_1)$, $z > 0$ (or $z = 0$ for a rectangular wedge) with out-of-plane normal $\tilde{N}_\beta = (0, \cos(\theta_1), -\sin(\theta_1))$. This gives rise to an additional term on the right-hand side of Eq. (2.15) for wedge 1,

$$\sum_{m,n=0}^{\infty} \frac{1}{\det(\mathbf{S}_1)} (M_{pq,mn}^{(\alpha\mu,1)} - \rho_1 v^2 \delta_{\alpha\mu}\delta_{pm}\delta_{qn})\, a_{mn}^{(\mu,1)} = \tau_q^{(\alpha,1)} + \tilde{\tau}_p^{(\alpha,1)}, \tag{2.28}$$

with "external stress amplitudes"

$$\tilde{\tau}_n^{(\alpha,1)} = \int_0^\infty \phi_n(ka_c^{(1)}\chi(\gamma_1)s)\, \tilde{N}_\beta^{(1)}\; T_{\alpha\beta}^{(\mathrm{ext})}(s\sin(\theta), s\cos(\theta)|k)\, ds. \tag{2.29}$$

Instead of (2.23) we have

$$U_n^{(\alpha,2)} = -\frac{\det(\mathbf{S}_1)}{b_c^{(1)}\,\chi(\gamma_1)} \sum_{q=0}^{\infty} G_{nq}^{(\alpha\beta,1)}(v^2)\tau_q^{(\beta,2)} + \frac{\det(\mathbf{S}_1)}{b_c^{(1)}\,\chi(\gamma_1)} \sum_{q=0}^{\infty} \tilde{G}_{nq}^{(\alpha\beta,1)}(v^2)\tilde{\tau}_q^{(\beta,1)} \tag{2.30}$$

with the new "Green's tensor"

$$\tilde{G}_{nq}^{(\alpha\beta)}(v^2) = \sum_{j=1}^{j_{\max}} \frac{Q_n^{(\alpha)}(j)\, \tilde{Q}_q^{(\beta)*}(j)}{\lambda(j) - \rho v^2}, \tag{2.31}$$

where

$$\tilde{Q}_m^{(\alpha)}(j) = \sum_{n=0}^{n_{\max}} V_{mn}^{(\alpha)}(j) \tag{2.32}$$

and $\lambda(j)$, $\mathbf{V}(j)$ are the j-th eigenvalue and eigenvector of the matrix $\mathbf{M}$. Using the condition $b_c^{(1)}\chi(\gamma_1) = b_c^{(2)}\chi(\gamma_2)$ and taking into account equation (2.24), we finally arrive at the inhomogeneous system of linear equations

$$[\mathbf{G}^{(1)-1}(v^2)/\det(\mathbf{S}_1) + \mathbf{G}^{(2)-1}(v^2)/\det(\mathbf{S}_2)]\,\mathbf{U}^{(1)} = \frac{1}{b_c^{(1)}\,\chi(\gamma_1)}\, \mathbf{G}^{(1)-1}\tilde{\mathbf{G}}^{(1)}\tilde{\boldsymbol{\tau}}^{(1)}, \tag{2.33}$$

where we have extended our short-hand notation of (2.25) to vectors $\mathbf{U}^{(1)}$, $\tilde{\boldsymbol{\tau}}^{(1)}$ standing for $(U_n^{(\alpha,1)})$, $(\tilde{\tau}_n^{(\alpha,1)})$, respectively.

2.2.3. Intermediate layer

The approach outlined above may also be applied to the system Fig. 1e, containing an intermediate layer of thickness $2d$ between two wedge-shaped elastic media. While in the two wedge-shaped regions, the displacement field is expanded in products of two Laguerre functions, (2.10), where $\eta_{1/2}$, $\zeta_{1/2}$ are now defined as

$$\begin{pmatrix} x \\ \eta_{1/2}(y,z) \\ \zeta_{1/2}(y,z) \end{pmatrix} = \mathbf{S}_{1/2}\mathbf{R}(\gamma_{1/2})\boldsymbol{\Gamma}_{1/2} \begin{pmatrix} x \\ y \mp d \\ z \end{pmatrix} = \mathbf{B}_{1/2} \begin{pmatrix} x \\ y \mp d \\ z \end{pmatrix}, \tag{2.34}$$

we follow [20] and expand the field in the intermediate layer in products of Laguerre functions and Legendre polynomials,

$$U_\alpha^{(3)}(y, z|k) = \sum_{m,n=0}^{\infty} a_{mn}^{(\alpha,3)}\; \tilde{P}_m(k\eta_3(y,z))\; \phi_n(k\zeta_3(y,z)) \tag{2.35}$$

with

$$\begin{pmatrix} x \\ \eta_3(y,z) \\ \zeta_3(y,z) \end{pmatrix} = \mathbf{B}_3 \begin{pmatrix} x \\ y \\ z \end{pmatrix} \tag{2.36}$$

and

$$\mathbf{B}_3 = \begin{pmatrix} 1 & 0 & 0 \\ 0 & 1/kd & 0 \\ 0 & 0 & b_c^{(3)} \end{pmatrix}. \tag{2.37}$$

The definition of the polynomials $\tilde{P}_n(\xi)$ differs from the usual definition of the Legendre polynomials by their normalization,

$$\int_{-1}^{1} \tilde{P}_m(\xi)\tilde{P}_n(\xi)\, d\xi = \delta_{mn}. \tag{2.38}$$

In addition to (2.15) with (2.16) we obtain analogous equations for the center part of the structure,

$$\sum_{m,n=0}^{\infty} \frac{1}{\det(\mathbf{B}_3)} (M_{pq,mn}^{(\alpha\mu,3)} - \rho_3 v^2 \delta_{\alpha\mu}\delta_{pm}\delta_{qn})\, a_{mn}^{(\mu,3)} = \tilde{P}_p(1)\,\tau_q^{(\alpha,R)} + \tilde{P}_p(-1)\,\tau_q^{(\alpha,L)} \tag{2.39}$$

with

$$M_{pq,mn}^{(\alpha\mu,3)} = \int_0^\infty \int_0^\infty [\tilde{D}_{\beta'}(k)\tilde{P}_p(k\eta)\phi_q(k\zeta)]^*\, \tilde{C}_{\alpha\beta'\mu\nu'}^{(3)}(kd)\, [\tilde{D}_{\nu'}(k)\tilde{P}_m(k\eta)\phi_n(k\zeta)]\, d\eta\, d\zeta, \tag{2.40}$$

where $\tilde{C}_{\alpha\beta'\mu\nu'}^{(3)}(kd) = B_{\beta'\beta}^{(3)}(kd)B_{\nu'\nu}^{(3)}(kd)C_{\alpha\beta\,\mu\nu}^{(3)}$, and we have defined the additional "stress amplitudes at the interfaces"

$$\tau_n^{(\alpha,R/L)} = \int_0^\infty \phi_n(kb_c^{(3)}z)\, N_\beta^{(R/L)}\; T_{\alpha\beta}^{(3)}(\pm d, z|k)\, dz. \tag{2.41}$$

In (2.41), $N_\beta^{(R/L)} = \pm\delta_{\beta 2}$ are the Cartesian components of unit vectors normal to the right/left interface and $\exp(ikx - \omega t)\, T_{\alpha\beta}^{(3)}(y, z|k)$ are the components of the stress tensor in the intermediate layer. Choosing the parameters $b_c^{(1)}$, $b_c^{(2)}$, $b_c^{(3)}$ such that $b_c^{(1)}\chi(\gamma_1) = b_c^{(2)}\chi(\gamma_2) = b_c^{(3)}$ and taking into account the boundary conditions for the stress at the interfaces, $N_\beta^{(L)}[T_{\alpha\beta}^{(2)}(-d, z|k) - T_{\alpha\beta}^{(3)}(-d, z|k)] = 0$, $N_\beta^{(R)}[T_{\alpha\beta}^{(1)}(d, z|k) - T_{\alpha\beta}^{(3)}(d, z|k)] = 0$, we obtain

$$\tau_n^{(\alpha,1)} = -\tau_n^{(\alpha,R)}, \quad \tau_n^{(\alpha,L)} = -\tau_n^{(\alpha,2)}. \tag{2.42}$$

Additional "displacement amplitudes at the interfaces" are defined via

$$U_n^{(\alpha,R/L)} = k\int_0^\infty \phi_n(kb_c^{(3)}z)\, U_\alpha^{(3)}(\pm d, z|k)\, dz = \frac{1}{b_c^{(3)}} \sum_{m=0}^{\infty} a_{mn}^{(\alpha,3)}\; \tilde{P}_m(\pm 1). \tag{2.43}$$

The continuity of the displacement field at the interfaces, $U_\alpha^{(2)}(-d, z|k) = U_\alpha^{(3)}(-d, z|k)$, $U_\alpha^{(1)}(d, z|k) = U_\alpha^{(3)}(d, z|k)$, leads to

$$U_n^{(\alpha,1)} = U_n^{(\alpha,R)}, \quad U_n^{(\alpha,L)} = U_n^{(\alpha,2)}. \tag{2.44}$$

Eliminating from (2.15), (2.21), (2.39) and (2.43) the expansion coefficients $a_{mn}^{(\alpha)}$ yields a homogeneous linear system of equations for the stress and strain amplitudes at the interfaces, namely

$$U_n^{(\alpha,R)} = -\frac{\det(\mathbf{S}_1)}{b_c^{(1)}\,\chi(\gamma_1)} \sum_{q=0}^{\infty} G_{nq}^{(\alpha\beta,1)}(v^2)\, \tau_q^{(\beta,R)}, \tag{2.45}$$

$$U_n^{(\alpha,L)} = -\frac{\det(\mathbf{S}_2)}{b_c^{(2)}\,\chi(\gamma_2)} \sum_{q=0}^{\infty} G_{nq}^{(\alpha\beta,2)}(v^2)\,\tau_q^{(\beta,L)}, \tag{2.46}$$

$$U_n^{(\alpha,L)} = \frac{\det(\mathbf{B}_3)}{b_c^{(3)}} \sum_{q=0}^{\infty} \left(\overset{-+}{G}{}_{nq}^{(\alpha\beta)}(v^2)\,\tau_q^{(\beta,R)} + \overset{--}{G}{}_{nq}^{(\alpha\beta)}(v^2)\,\tau_q^{(\beta,L)}\right), \tag{2.47}$$

$$U_n^{(\alpha,R)} = \frac{\det(\mathbf{B}_3)}{b_c^{(3)}} \sum_{q=0}^{\infty} \left(\overset{++}{G}{}_{nq}^{(\alpha\beta)}(v^2)\,\tau_q^{(\beta,R)} + \overset{+-}{G}{}_{nq}^{(\alpha\beta)}(v^2)\,\tau_q^{(\beta,L)}\right). \tag{2.48}$$

The matrices $(\overset{\sigma\sigma'\alpha\beta}{G}{}_{mn})$, where $\sigma,\ \sigma'$ stand for the signs + or −, are evaluated in terms of eigenvectors $\mathbf{V}^{(3)}(j)$ and eigenvalues $\lambda_3(j)$ of the matrix $\mathbf{M}^{(3)}$ after truncation of the series (2.35) as

$$\overset{\sigma\sigma'(\alpha\beta)}{G}{}_{mn}(v^2) = \sum_{j=1}^{j_{\max}} \frac{\overset{\sigma(\alpha)}{Q}{}_m(j)\ \overset{\sigma'(\beta)*}{Q}{}_n(j)}{\lambda_3(j) - \rho_3 v^2}, \tag{2.49}$$

$$\overset{\sigma(\alpha)}{Q}{}_n(j) = \sum_{m=0}^{m_{\max}} V_{mn}^{(\alpha,3)}(j)\,\tilde{P}_m(\sigma 1). \tag{2.50}$$

The maximum number of Legendre polynomials in (2.35) is $m_{\max} + 1$, the maximum number of Laguerre functions $n_{\max} + 1$, and consequently $j_{\max} = 3(m_{\max} + 1)(n_{\max} + 1)$. From (2.45)–(2.48) the following secular equation is readily derived:

$$\det\begin{pmatrix} \frac{\det(\mathbf{B}_3)}{\det(\mathbf{S}_1)}\overset{-+}{\mathbf{G}}(\mathbf{G}^{(1)})^{-1} & \frac{\det(\mathbf{B}_3)}{\det(\mathbf{S}_2)}\overset{--}{\mathbf{G}}(\mathbf{G}^{(2)})^{-1} + \mathbf{I} \\ \frac{\det(\mathbf{B}_3)}{\det(\boldsymbol{S}_1)}\overset{++}{\mathbf{G}}(\mathbf{G}^{(1)})^{-1} + \mathbf{I} & \frac{\det(\mathbf{B}_3)}{\det(\boldsymbol{S}_2)}\overset{+-}{\mathbf{G}}(\mathbf{G}^{(2)})^{-1} \end{pmatrix} = 0. \tag{2.51}$$

It is straightforward to introduce an external source in this system consisting of three media in the same way as outlined in the preceding subsection. In our numerical calculations, a typical maximal number of Laguerre functions and Legendre polynomials was 30.

2.3. Validation of the two approaches

In order to avoid wrong conclusions due to lack of accuracy, convergence problems or in the case of FEM calculations, a non-optimal choice of mesh, system size or PML parameters, the two methods have been applied to the same system in certain cases, and agreement has been found. The convergence of the two methods is demonstrated for the example of a system corresponding to Fig. 1e.

The media on the right and left (1 and 2 in Fig. 1e) were chosen to be both aluminum (for material constants see Table 1), the medium in the center consisted of a test material with properties partly similar to those of copper (Table 1), the two angles are $\theta_1 = 45^\circ$, $\theta_2 = 40^\circ$. The 1D wave-vector k was equal to $1/(2d)$.

For the FEM calculations, meshes of the form of Fig. 2c were used. In addition, a mesh was set up with the following property: The x_3-coordinates of the node positions increase logarithmically along the x_3-axis away from the free surfaces. Also, the moduli of the x_2-coordinates of the nodes in the media on the left and right increase logarithmically with increasing distance from the center medium (Fig. 2d). In these tests, the displacements at the bottom, on the left and on the right edges of the mesh were set equal to zero.

The data in Fig. 4 demonstrate that the two methods converge to the same value of the phase velocity of the guided wave if the element size in the FEM calculation at the surface of the center region is sufficiently small. They also show that meshes with a logarithmic increase of element size away from the surface of the center region (Fig. 2d) lead to much faster convergence than the linear meshes of Fig. 2c. This is because the spatial variations of the displacement field associated with the guided waves become less rapid with increasing distance from the top center of the structure. The logarithmic stretching of the elements was arranged such that for the case of 70 elements aligned along the x_3-axis in the center region, the distance between the surface and the bottom of the center medium is five times longer for the logarithmically stretched mesh as compared to the linear mesh. The results in Fig. 4 also point to a significant influence of the convergence factors a_c, b_c occurring in the Laguerre functions. With a proper choice of these factors, the convergence can be much enhanced and very accurate values for the phase velocity ($< 0.02\%$) can be obtained with less than 11 Laguerre functions and Legendre polynomials.

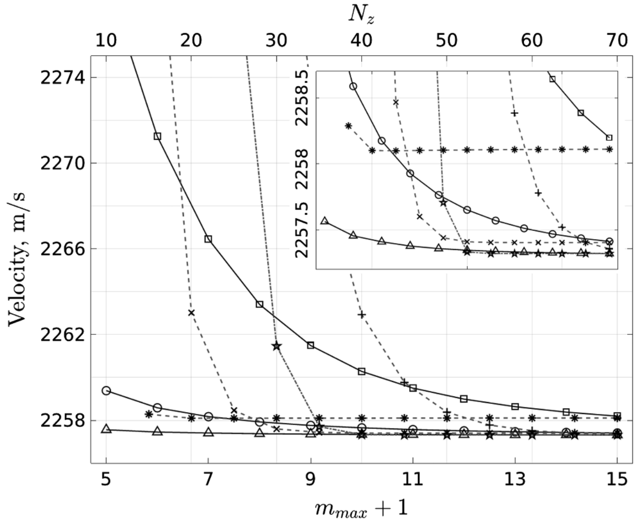

Fig. 4. Convergence of the speed of the slowest 1D guided mode in the system shown in Fig. 1e, where $\theta_1 = 45^\circ$ and $\theta_2 = 40^\circ$. Solid lines: Laguerre-Legendre function method with three different sets of convergence factors. $a_c^{(1)} = 0.5$ (squares), 1.0 (circles), 2.0 (triangles). $b_c^{(1)} = a_c^{(1)}$, $b_c^{(2)} = a_c^{(2)} = a_c^{(1)}\chi(\gamma_1)/\chi(\gamma_2) \approx 1.08\,a_c^{(1)}$, $m_{\max}$: highest index of Laguerre functions and Legendre polynomials employed in the calculation. Dashed lines: FEM calculations with meshes of the form shown in Fig. 2c. N: Number of elements along the x_3-axis (see Fig. 2). $k\Delta = 0.5$ (*), 0.25 (x), 0.125 (+), where Δ is the edge length of a square element at the surface of the center medium. Dashed-dotted line/stars: logarithmic mesh (Fig. 2d) with $k\Delta = 0.125$. For more explanations see text in Subsection 2.3 and definitions in Subsection 2.2.

Table 1
Material data used in the numerical calculations.

	ρ [kg/m^3]	λ [GPa]	μ [GPa]	v_L [m/s]	v_T [m/s]	v_R [m/s]
Aluminium	2712	61.4	25.0	6409.1	3036.2	2841.2
Copper	8900	98.32	46.27	4630.8	2280.1	2128.5
Test Material	8900	56.0	56.0	4344.7	2508.4	2306.2
PMMA	1190	3.0	1.5	2245.4	1122.7	1047.0

3. Numerical results

3.1. Two media in contact

In [11], it was shown that 1D guided acoustic waves exist at the intersection of the interface between two elastic quarter-spaces and their common surface (Fig. 1a). In particular, the case has been considered that both elastic media in this structure are Poisson media, i.e. isotropic materials with their two Lamé constants λ, μ being equal. The parameter space is then two-dimensional, and the two parameters may be chosen as ρ′/ρ and μ'/μ, where ρ′, ρ are the mass densities and μ', μ the shear moduli of medium 1 and medium 2, respectively. For this case, Scholte [12] determined the existence domain of Stoneley waves, i.e. acoustic waves being localized at the interface between two elastic half-spaces. In [11] the domain of existence in the two-dimensional parameter space was determined and found to be a small subset of the existence domain of Stoneley waves.

We now consider an interface between the two media which is no

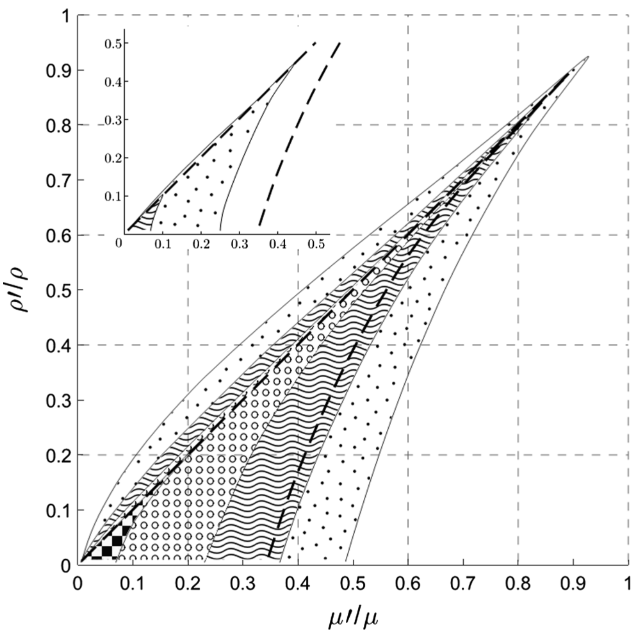

Fig. 5. Existence domain of 1D guided modes in structures corresponding to Fig. 1b made of two Poisson media with densities ρ, ρ′ and shear moduli μ, μ'. Angles $\theta = 90^\circ$ (filled squares), 70° (open circles), 50° (wavy lines), 30° (dots). Existence domains for larger angles are subsets of those for smaller angles. Dashed lines: boundary of the existence domain of Stoneley waves. Inset: Existence domain of second mode for angles θ = 50° (wavy lines), 30° (dots).

longer vertical to the surface (Fig. 1b). With decreasing inclination angle θ, the domain of existence of 1D guided modes widens, and for $\theta < 50^\circ$ it contains the existence area of Stoneley waves in the 2D parameter space (Fig. 5).

With decreasing angle θ, a small domain opens up in the parameter space where a second 1D guided mode exists. Like the existence domain of the first mode, it widens as θ becomes smaller (Inset of Fig. 5).

In Fig. 6, displacement patterns, determined in FEM calculations, of the first and second modes are shown for a certain combination of parameters. The components U_2 and U_3 are exhibited which can be chosen to be both real. The high degree of localization of the intersection between the surface and the interface is due to the low velocity of this mode, υ_1, as compared to the lowest of the Rayleigh velocities, υ_{Rmin}, of the two media, $\upsilon_1/\upsilon_{\mathrm{Rmin}} = 0.82$, and to the Stoneley wave velocity, υ_{S}, $\upsilon_1/\upsilon_{\mathrm{S}} = 0.79$. The second mode is much less localized, both along the surface and along the interface, since its velocity, υ_2, is much closer to the lowest of the two Rayleigh velocities, $\upsilon_2/\upsilon_{\mathrm{Rmin}} = 0.98$. Its displacement pattern is more complex as compared to that of the first mode, exhibiting a node in the directions along the surface and the interface.

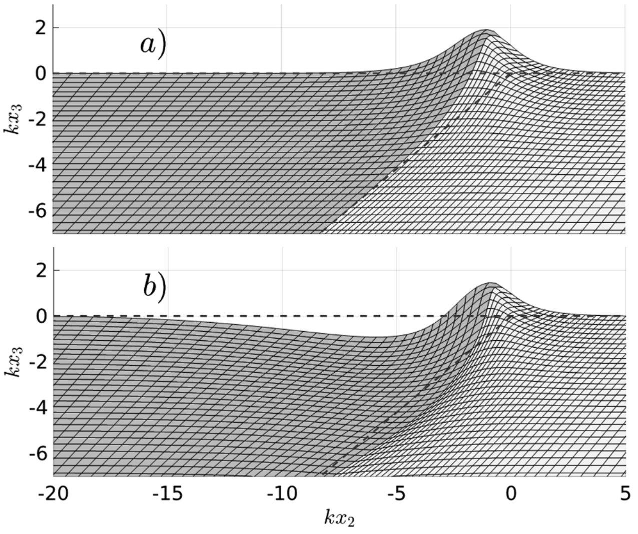

Fig. 6. Displacements for first (upper) and second (lower) modes. Angle $\theta = 40^\circ$, $\mu'/\mu = 0.08$, $\rho'/\rho = 0.05$. Dashed lines: surface and interface in the undeformed state. The displacement component along the x_1-direction is not shown.

In the limit $\rho'/\rho \to 1$ and $\mu'/\mu \to 1$, the two media in Fig. 1b become equal and form a homogeneous isotropic half-space, where 1D guided acoustic waves do not exist. On the other hand, as ρ'/ρ and μ'/μ both tend to zero, the effect of the lighter and softer of the two wedges forming the half-space in Fig. 1b becomes negligible, and the 1D guided modes in this limit are the wedge waves of the heavier and stiffer material.

A different way of enlarging the existence range of 1D non-dispersive acoustic modes guided by the intersection of an interface and the surfaces of two elastic media is shown in Fig. 1c. By reducing the angle θ to less than 90°, the structure becomes a composite wedge with decreasing opening angle. For the case of both materials being Poisson media, the existence ranges of the 1D guided waves, localized at the apex of the composite wedge, are shown for various angles θ in Fig. 7. The shape of the existence regions clearly differs from those shown in Fig. 5, since in the systems of Fig. 1c, 1D guided waves exist also in the case of both materials being equal. Below a certain wedge angle, they are the asymmetric flexural wedge waves localized at the apex of homogeneous wedges.

For a particular material combination (aluminum and copper), the phase velocities of 1D guided waves in composite wedges of the type of Fig. 1c are shown along with the velocities of wedge waves in homogeneous aluminum and copper wedges (Fig. 8). The material parameters used are listed in Table 1.

Since the Poisson ratios of aluminum and copper are almost equal, wedge wave branches for the homogeneous media emerge at the same wedge angles. For the composite wedges, corresponding branches appear below the smallest of the two Rayleigh velocities at slightly smaller wedge angles as compared to the homogeneous wedges. (Note that

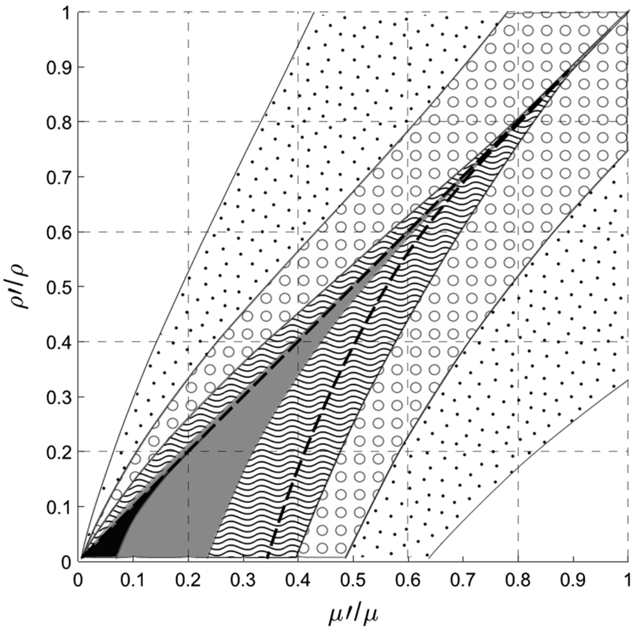

Fig. 7. Existence domain of 1D guided modes in structures corresponding to Fig. 1c made of two Poisson media with densities ρ, ρ′ and shear moduli μ, μ'. Angles $\theta = 90^\circ$ (black), 70° (grey), 50° (wavy lines), 40° (open circles), 30° (dots). Existence domains for larger angles are subsets of those for smaller angles. Dashed lines: boundary of the existence domain of Stoneley waves.

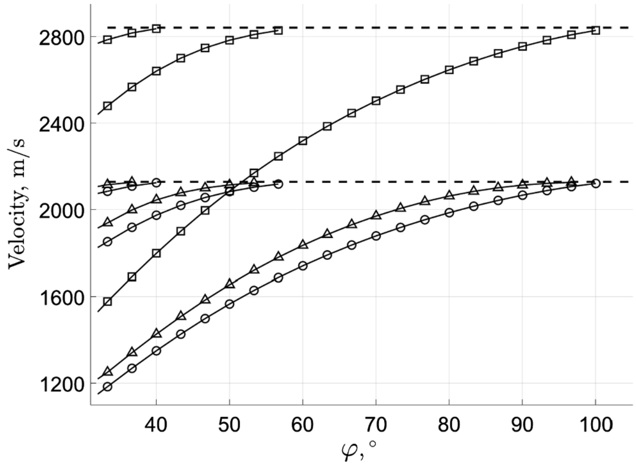

Fig. 8. Velocity of wedge waves in aluminum (squares), copper (circles) and composite wedges (Fig. 1c) made of aluminum and copper (triangles), as function of the opening angle φ of the wedge. $\varphi = 2\theta$. Upper/lower dashed line: Rayleigh wave velocity in aluminum/copper.

$\varphi = 2\theta$).

In addition to fully localized 1D guided modes with exponential decay for $x_2^2 + x_3^2 \to \infty$, leaky waves exist in composite wedges of the form Fig. 1d made of two isotropic materials. Leaky wedge waves were first found in laser-ultrasound experiments in Si wedges which exhibit a high degree of anisotropy [13]. In numerical calculations, it was shown that such leaky waves exist in composite wedges even if these are made of two isotropic materials [14]. As example systems we consider here composite wedges made of two materials with strong acoustic mismatch, namely aluminum and PMMA. In the FEM calculations, a time-harmonic driving force was applied to the top node of the 2D mesh at the tip of the wedge, for simplicity. This force had Cartesian components of equal size with respect to the coordinate system in Fig. 1. In Fig. 9, twice the logarithm of the magnitude of the displacement vector, $\sqrt{U_1^2 + U_2^2 + U_3^2}$ is shown as function of the velocity (ω/k) and one of the two angles θ_1, θ_2 (Fig. 1d), while the other angle is fixed at the arbitrary value of 30°. Branches of resonances with velocities above the Rayleigh wave and bulk shear wave velocities in PMMA are clearly visible. They correspond to leaky waves that radiate energy away from the tip of the composite wedge into the PMMA. For angles $\theta_2 > 30°$, the resonance becomes very weak and disappears as θ_2 further increases. With decreasing angle θ_2, the resonance becomes sharper indicating that the leaky wave should be more strongly localized at the wedge tip. As θ_2 tends to zero, the role of the PMMA part of the composite Al/PMMA wedge reduces to a small perturbation on one of the surfaces of an Al wedge, and the leaky wave velocity converges to the velocity of fully tip-localized wedge waves of an Al wedge with opening angle of 30° (1436.5 m/s) as displayed in Fig. 8.

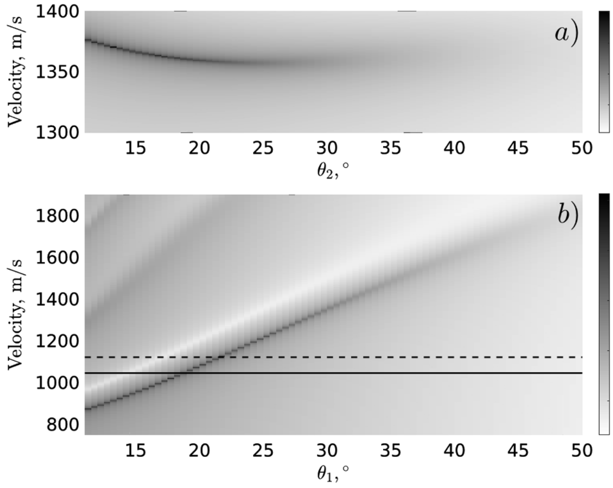

Fig. 9. Magnitude of displacement vector at the tip of a composite wedge (Fig. 1d) consisting of aluminum (material 1) and PMMA (material 2) (greyscale proportional to $\log(U_1^2 + U_2^2 + U_3^2)$). $\theta_1 = 30°$ (a), $\theta_2 = 30°$ (b). Solid line: Rayleigh wave velocity, dashed line: Bulk shear wave velocity of PMMA, respectively (see Table 1).

In Fig. 9b, a branch of pronounced resonances is detected which weakens for angles θ_1 of the aluminum partial wedge larger than 35°. For θ_1 less than 22°, the velocities corresponding to this branch become smaller than the bulk shear wave velocity of PMMA, which means that the leaky waves can radiate energy away from the tip only via surface waves propagating on the surface of the PMMA partial wedge. (Note that at the PMMA/aluminum interface, Stoneley waves do not exist.) At approximately 18° the branch merges into the non-radiative region below the Rayleigh wave velocity of PMMA and now represents perfectly tip-localized wedge waves.

Two more leaky wave branches are visible in Fig. 9b, albeit less pronounced than the lowest one. As θ_1 tends to zero, the velocities of the two lowest branches seem to converge to the velocities of the fully localized wedge waves in PMMA wedges with opening angle of 30°.

3.2. Three media in contact

Systems of the form of Fig. 1e may be regarded as two quarter-spaces or two wedge-shaped elastic media which are not directly connected (welded), but linked via a third medium in the form of an elastic plate. Such structures obviously find realizations in various contexts, for example two components of a technical device, which are linked by an elastic bond, e.g. an adhesive layer, or two pieces of rock with a gap in between, filled by another material.

We confine ourselves here to an example with media 1 and 2 in Fig. 1e being identical. For the outer material, aluminum and for the center material, copper was chosen. While the elastic constants of both media are of comparable size, the center material is much heavier than the outer material. This causes the bulk-wave and Rayleigh wave velocities of the center material to be smaller than those of the outer medium (see Table 1). The outer medium, has the shape of two wedges with opening angles $\theta_1 = \theta_2 = 40°$. Dispersion curves for 1D guided waves localized at the surface of the center medium of this structure are shown in Fig. 10 along with displacement patterns in the x_2-x_3 plane. The Rayleigh wave velocity of aluminum is larger than the bulk shear wave velocity v_T of copper. In an infinite copper plate in welded contact with aluminum half-spaces at its upper and lower surfaces, monochromatic guided acoustic waves exist with displacement field decaying exponentially into the aluminum half-spaces. We call them generalized plate modes as they may be regarded as analogs of Lamb waves in a free-standing infinite plate. Their speeds are always larger than v_T and, for certain branches of their dispersion relation, tend to v_T with decreasing wavelength. This has been verified numerically for the lowest branches using the material constants of Cu and Al given in Table 1. From this fact we may conclude that all modes with velocities smaller than v_T (upper horizontal line in Fig. 10) are guided at the surface of the center medium ($x_3 = 0$). This means that their associated displacements decay exponentially into the depth of the center medium and in the outer medium away from the interfaces. Also note that Stoneley waves do not exist at a planar interface between a copper and an aluminum half-space.

Acoustic waves propagating along the surface of the center medium with velocity v higher than v_T are expected to be leaky. However they may still be fully guided in special cases, since the existence of bulk waves or of the above-mentioned generalized plate modes with speeds smaller than v at sufficiently small wavelength is only a necessary, not a sufficient condition for leakage.

The guided modes in this system may be characterized by their

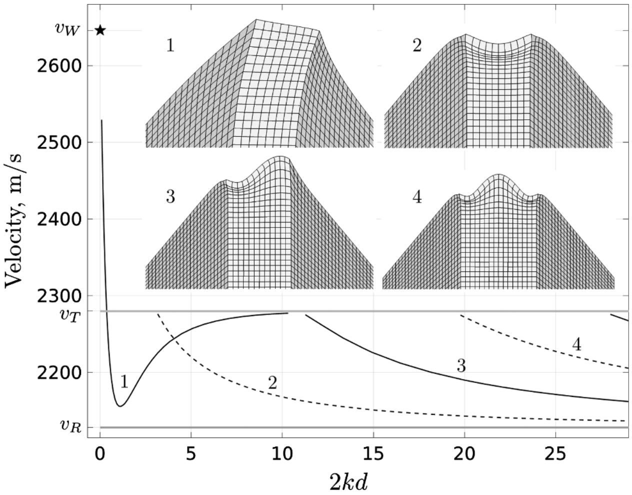

Fig. 10. Dispersion relation (phase velocity as function of wave-vector k) of 1D guided modes of odd (solid) and even (dashed) symmetry in a system of form Fig. 1e with $\theta_1 = \theta_2 = 40°$, medium 1 and 2: aluminum, medium 3: copper. Upper horizontal line: Velocity of bulk transverse waves in copper. Lower horizontal line: Rayleigh wave velocity of copper. Insets: Displacement patterns in the x_2-x_3 plane of modes of branch 1 at $2kd = 3$, branch 2 at $2kd = 8$, branch 3 at $2kd = 15$ and branch 4 at $2kd = 25$. For material data see Table 1. v_W: Velocity of wedge wave propagating in an aluminum wedge with opening angle of 80°.

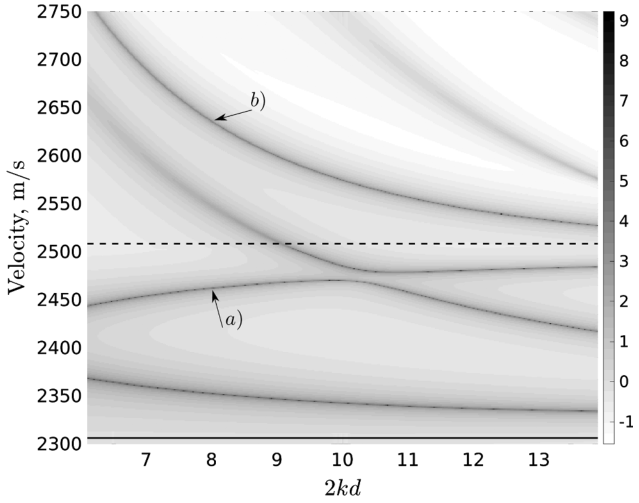

Fig. 11. Mean square of displacement vector at the surface of medium 3 in the structure Fig. 1e with $\theta_1 = \theta_2 = 40°$, medium 1 and 2: aluminum, medium 3: test material. (For material data see Table 1.) Greyscale proportional to $\log[\sum (U_1^2 + U_2^2 + U_3^2)]$, where $\sum (U_1^2 + U_2^2 + U_3^2)$ is the sum over the squares of displacement magnitudes of all nodes on the surface of medium 3 in the FEM calculation. Solid line: Rayleigh wave velocity, dashed line: Bulk shear wave velocity of medium 3. The arrows refer to the displacement patterns displayed in Fig. 12.

symmetry with respect to reflection at the x_1-x_3 plane. With increasing magnitude of the wave-vector k along the x_1-direction, new dispersion branches of guided waves with alternating symmetry emerge in the velocity interval between v_T and the Rayleigh wave velocity v_R of the center material. The inset of Fig. 10 exhibits the displacement patterns of modes belonging to the first four branches. They are guided by the surface of the center medium. While propagating in the x_1-direction and decaying to zero in the x_3-direction and in the outer media, they are of standing-wave character along the x_2-axis (Fig. 1) with number of nodes increasing with increasing branch number. As the angles θ_1, θ_2 of the outer aluminum wedges approach zero, these modes are expected to tend to the well-known edge modes of a plate ([20,28–30] and the recent review [31] with further references).

The displacement pattern of the first mode shown in the inset of Fig. 10 contains a considerable amount of strain in the aluminum wedges. In fact, the displacement field of the first mode, corresponding to a phase velocity of 2221.2 m/s, resembles that of an anti-symmetric flexural wedge wave. A remarkable feature of the first branch of the dispersion relation in Fig. 10 is its steep minimum and the very rapid increase of the phase velocity with decreasing values of kd, i.e. with increasing wavelength or decreasing thickness of the intermediate copper layer between the two aluminum wedges. At $2kd \approx 0.4$ the phase velocity of this mode reaches the velocity of bulk shear waves in the center medium. For smaller values of $2kd$ the waves are expected to become leaky. In Fig. 10, this dispersion branch is continued into the radiative regime above v_T by FEM calculations by solving the eigenvalue problem (2.9) for a system of finite extension in the x_2-x_3 plane and with a source and perfectly matched layers. The dispersion curves obtained in these two ways agree very well, indicating that the leakage of this mode with velocities $> v_T$ is very small. In Fig. 10, the dispersion branch is truncated for reasons of numerical inaccuracy and mixing with bulk resonances. In the limit $kd \to 0$ we expect the phase velocity of the first mode to converge to the value of the wedge wave velocity in a pure aluminum wedge without intermediate copper layer and opening angle $\theta_1 + \theta_2 = 80°$ (2646.2 m/s).

The steep increase of the dispersion curve of the first mode in Fig. 10, both in the non-radiative and in the radiative regime, may be used as a sensitive tool to determine the thickness of intermediate layers or variations of this quantity.

We note here that a different scenario was observed for two quarter-spaces linked by an intermediate layer of a very soft material with thickness $2d$ (Fig. 1e with $\theta_1 = \theta_2 = 90°$) [32]. Here, the weak coupling between the two identical rectangular wedges, which is effectuated by the center material, leads to a splitting of the wedge wave velocity resulting in two close dispersion branches for symmetric and anti-symmetric modes.

Leaky waves in a system of the type of Fig. 1e have been investigated in more detail in FEM calculations with a source which consisted in a time-harmonic traction on the left half of the surface of the intermediate layer. In this area of the surface, the traction vector had constant amplitude and the magnitudes of its three components were equal. Results of these calculations are shown in Fig. 11. In comparison to the data in Fig. 10, different material constants were used for the intermediate layer (test material in Table 1). The dispersion relation in the non-radiative regime between the solid and dashed horizontal lines differs markedly from the corresponding curves in Fig. 10, which points to its sensitivity to the elastic properties of the intermediate layer. For example, an avoided crossing occurs of two dispersion branches belonging to modes of like symmetry, corresponding to branches 1 and 3 in Fig. 10.

Equally remarkable are the very well pronounced leaky wave branches above the dashed horizontal line which indicates a high degree of localization at the surface of medium 3. For an infinite plate with material constants corresponding to the test material in Table 1, sandwiched between two aluminum half spaces in welded contact, generalized plate modes exist having speeds that converge from below to the bulk shear wave velocity of the test material with decreasing wavelength. This implies that the modes in Fig. 11 with velocities slightly below the dashed line may be leaky, too.

In Fig. 12b, the displacement profile of a leaky wave with velocity $v = 2635.3$ m/s, along the x_3-axis normal to the surface in the center of medium 3 (Fig. 1e) is shown and compared to the displacements of a fully localized anti-symmetric 1D guided mode (Fig. 12a). Near the surface, the displacement amplitudes are much larger than those of the radiation part in the depth of the intermediate layer. The decay of the displacements for $kx_3 > 80$ occurs in the perfectly matched layer. The fact that the magnitude of the vector (U_1, U_2, U_3) is independent of x_3 in

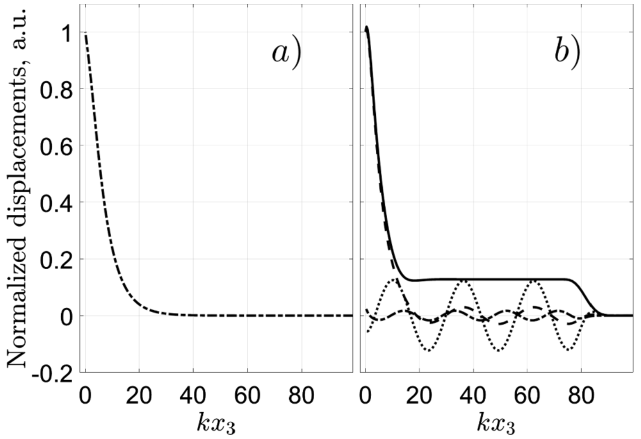

Fig. 12. Displacement field of 1D guided mode with velocity $v = 2461.8$ m/s (a) and leaky wave with velocity $v = 2635.3$ m/s (b) on the midplane (x_1-x_3 plane) of the intermediate layer (medium 3 in Fig. 1e), $2kd = 8$. The two modes are indicated on the dispersion relation in Fig. 11 by arrows. Real parts of U_1 (dashed), U_2 (dashed-dotted), U_3 (dotted), $\sqrt{U_1^2 + U_2^2 + U_3^2}$ (solid). Normalization such that $\sqrt{U_1^2 + U_2^2 + U_3^2} = 1$ at the surface ($x_3 = 0$) and $U_2(x_3 = 0)$ real.

the interval $20 < kx_3 < 70$ indicates that the perfectly matched layer has efficiently suppressed wave components reflected from the bottom of the structure [21].

4. Conclusions

At the intersection of planar surfaces and interfaces of elastic media and in structures consisting of two wedge-shaped solids linked by an elastic layer, one-dimensional guided acoustic waves have been found and some of their properties described. The displacement fields of properly 1D guided waves decay exponentially in two spatial dimensions. In addition to these fully guided waves, various leaky wave branches were found with a high degree of localization at the intersection line of surfaces and an interface or at the surface of an intermediate layer between two wedge-type solids. Both the fully guided and the leaky 1D guided waves may be applied in non-destructive inspection of the edges of interfaces and intermediate layers in technical devices, for example. In a specific system it was shown that their dispersion relation can be highly sensitive to variations of material properties and geometry. For this reason, along with their complex displacement patterns, they qualify for applications in non-destructive evaluation (NDE). With their complex displacement patterns, they should be well suited for the non-destructive detection of specific defects at interfaces. For example, one can envisage their use in early detection of incipient delamination at edges or surfaces of composite materials or structures with adhesive bonds. Since the penetration depth of the 1D guided waves from the edge into the interface of the two bonded media depends on their frequency, an inspection of parts of the interface with tunable sensitivity to depth could be achieved in principle. A further advantage of the 1D guided acoustic waves studied in this work, as compared to bulk or 2D guided waves like Rayleigh waves, is the absence of diffraction losses. Another field, where the geometries of Fig. 1 are of relevance are seismic waves propagating between two wedge-shaped rocks in contact. The contact could be mediated by an additional material filling a cleft between the two rocks.

Our investigations are based on two different computational approaches, a semi-analytical finite element method and an expansion of the displacement field in a double series of functions that are particularly suited to capture the essential features of the guided modes' displacement patterns in the systems considered here. In this work, the latter method has mainly been used to validate the prior. Clearly, the finite element method has a much higher flexibility with regard to the geometries it can be applied to and is easier to implement. However, the convergence of the alternative method can be tested more easily as it contains less parameters, and it allows to obtain results of very high accuracy with comparatively small numerical effort, if the convergence factors in this approach are well-chosen.

In our search for leaky waves, a spatially strongly localized source with specific polarization was applied and magnitudes of displacements in a confined surface area or at the tip of a wedge were scanned as functions of frequency. This procedure should be sufficient for detecting those leaky waves that are localized predominantly at the wedge tip or the surface area of the intermediate layer in the systems we have investigated here. A comprehensive study of leaky waves in these systems could be based on random sources along the path described in [33]. Alternative approaches to the ones discussed here are diffraction-theoretical methods used for the analysis of scattering of acoustic waves from wedge-shaped structures (see for example [34,35] and further references in [36]). As in the case of acoustic wedge waves (see for example the reviews [9,37]), analytic results for the displacement field and phase velocity of the guided waves are expected to be achievable only with the help of strong approximations. For wedge waves, rigorous existence proofs were given for isotropic media and certain anisotropic configurations in [38–40]. These authors applied a variational principle with test functions derived from the displacement field of surface acoustic waves. This approach may perhaps be extended to the systems of Fig. 1. However, with increasing complexity of the test functions, it will be difficult, if not impossible, to obtain analytic results for borders of existence in the parameter space, and a numerical approach, as pursued in this work, becomes inevitable.

Acknowledgement

The authors would like to thank Alexey Lomonosov, Peter Hess and Iren Kusnetsova for stimulating discussions and Deutsche Forschungsgemeinschaft for financial support (DFG Grant No. MA 1074/11-3). I.A. Nedospasov acknowledges the support of the Russian Basic Research Foundation (Grant Nos. 17-07-00608 and 16-07-00629).

References

[1] J.L. Rose, The upcoming revolution in ultrasonic guided waves, Proc. SPIE 7983 (2011) 798302-1–30.
[2] B.K. Sinha, S. Asvadurov, Dispersion and radial depth of investigation of borehole modes, Geophys. Prosp. 52 (2004) 271–286.
[3] M. Roth, K. Holliger, A.G. Green, Guided waves in near-surface seismic surveys, Geophys. Res. Lett. 25 (1998) 1071–1074.
[4] D. Royer, E. Dieulesaint, Elastic Waves in Solids II, Generation, Acousto-Optic Interaction, Applications, Springer, Berlin, 2000.
[5] A. Ruiz, P.B. Nagy, SAW dispersion measurements for ultrasonic characterization of surface treated metals, Instr. Meas. Metrol. 3 (2003) 59.
[6] K.H. Matlak, J.Y. Kim, L.J. Jacobs, J. Qu, Review of second harmonic generation measurement techniques for material state determination in metals, J. Nondestruct. Eval. 34 (2015) 273–296.
[7] M.J.S. Lowe, D.N. Alleyne, P. Cawley, Defect detection in pipes using guided waves, Ultrasonics 36 (1998) 147–154.
[8] H. Estrada, S. Gottschalk, M. Reiss, V. Neuschmelting, J. Rebling, R. Goldbrunner, D. Razansky, Looking at the skull in a new light: Rayleigh-Lamb waves in cranial bone, Proc. IEEE Ultrason. Symp. (2018).
[9] P. Hess, A.M. Lomonosov, A.P. Mayer, Laser-based linear and nonlinear guided elastic waves at surfaces (2D) and wedges (1D), Ultrasonics 54 (2014) 39–55.
[10] A.A. Oliner, Waveguides for surface waves, in: A.A. Oliner (Ed.), Acoustic Surface Waves, Springer, Berlin, 1978, pp. 187–223.
[11] E.S. Sokolova, A.S. Kovalev, A.A. Maznev, A.P. Mayer, Acoustic waves guided by the intersection of a surface and an interface of two elastic media, Wave Motion 49 (2012) 388–393.
[12] J.G. Scholte, The range and existence of Rayleigh and Stoneley waves, Mon. Not. R. Astron. Soc.: Geophys. (Suppl. 5) (1947) 120–126.
[13] A.M. Lomonosov, P. Hess, A.P. Mayer, Silicon edges as one-dimensional waveguides for dispersion-free and supersonic leaky wedge waves, Appl. Phys. Lett. 101 (2012) 031904-1–4.
[14] P.D. Pupyrev, unpublished.
[15] B.C. Abell, L.J. Pyrak-Nolte, Coupled wedge waves, J. Acoust. Soc. Am. 134 (2013) 3551–3560.

[16] P.E. Lagasse, Analysis of a dispersion-free guide for elastic waves, Electron. Lett. 8 (1972) 372–373.

[17] P.E. Lagasse, Higher-order finite-element analysis of topographic guides supporting elastic surface waves, J. Acoust. Soc. Am. 53 (1973) 1116–1122.

[18] A.A. Maradudin, R.F. Wallis, D.L. Mills, R.L. Ballard, Vibrational edge modes in finite crystals, Phys. Rev. B 6 (1972) 1106–1111.

[19] S.L. Moss, A.A. Maradudin, S.L. Cunningham, Vibrational edge modes for wedges with arbitrary interior angles, Phys. Rev. B 8 (1973) 2999–3008.

[20] A.A. Maradudin, K.R. Subbaswamy, Edge localized vibration modes on a rectangular ridge, J. Appl. Phys. 48 (1977) 3410–3414.

[21] M. Mayer, S. Zaglmayr, K. Wagner, J. Schöberl, Perfectly matched layer finite element simulation of parasitic acoustic wave radiation in microacoustic devices, Proc. IEEE Ultrason. Symp. (2007) 702–706.

[22] T.M. Sharon, A.A. Maradudin, S.L. Cunningham, Vibrational edge modes for small-angle wedges, Phys. Rev. B 8 (1973) 6024–6026.

[23] T.M. Sharon, Edge modes for piezoelectric wedges of arbitrary interior angles, Proc. IEEE Ultrason. Symp. (1973) 126–130.

[24] S. Datta, B.J. Hunsinger, Analysis of line acoustical waves in general piezoelectric crystals, Phys. Rev. B 16 (1977) 4224–4229.

[25] P.D. Pupyrev, A.M. Lomonosov, P. Hess, A.P. Mayer, Symmetry effects on elastic wedge waves at anisotropic edges, J. Appl. Phys. 115 (2014) 243504-1–11.

[26] E.S. Sokolova, A.S. Kovalev, A.P. Mayer, Second-order nonlinearity of wedge acoustic waves in anisotropic media, Wave Motion 50 (2013) 246–252.

[27] B.C. Abell, D.D. Nolte, L.J. Pyrak-Nolte, Intersection waves, J. Geophys. Res.: Solid Earth 122 (2017) 7824–7838.

[28] R. Burridge, F.J. Sabina, Theoretical computations on ridge acoustic surface waves using the finite-element method, Electron. Lett. 7 (1971) 720–722.

[29] J.Y.H. Chu, C. Courtney, Ultrasonic edge waves for damage detection in composite plate stiffeners, Proc. IEEE Ultrason. Symp. (2016), https://doi.org/10.1109/ULTSYM.2016.7728688.

[30] F. Feng, Z. Shen, J. Shen, Edge waves in a 3D plate: Two solutions based on plate mode matching, Mathem. Mech. Solids 22 (2017) 2065–2074.

[31] J.B. Lawrie, J. Kaplunov, Edge waves and resonance on elastic structures: an overview, Mathem. Mech. Solids 17 (2012) 4–16.

[32] P.D. Pupyrev, E.S. Sokolova, A.P. Mayer, unpublished.

[33] V. Laude, M.E. Korotyaeva, Stochastic excitation method for calculating the resolvent band structure of periodic media and waveguides, Phys. Rev. B 97 (2018) 224110.

[34] B.V. Budaev, D.B. Bogy, Scattering of Rayleigh and Stoneley waves by two adhering elastic wedges, Wave Motion 33 (2001) 321–337.

[35] A.K. Gautesen, Scattering of Rayleigh wave by an elastic wedge whose angle is less than 180°, Wave Motion 36 (2002) 417–424.

[36] A.N. Darinskii, M. Weihnacht, H. Schmidt, FE analysis of surface acoustic wave transmission in composite piezoelectric wedge structures, Ultrasonics 84 (2018) 366–372.

[37] A.P. Mayer, V.V. Krylov, A.M. Lomonosov, Guided acoustic waves propagating at surfaces, interfaces, and edges, Proc. IEEE Ultrason. Symp. (2011) 2046–2052.

[38] I.V. Kamotskii, On a surface wave traveling along the edge of an elastic wedge, Algebra Analiz 20 (2008) 86–92.

[39] G.L. Zavorokhin, A.I. Nazarov, On elastic waves in a wedge, J. Math. Sci. 175 (2011) 646–650.

[40] P.D. Pupyrev, A.M. Lomonosov, A. Nikodijevic, A.P. Mayer, On the existence of guided acoustic waves at rectangular anisotropic edges, Ultrasonics 71 (2016) 278–287.